

Article

Solid Electrolyte Membranes Based on $\text{Li}_2\text{O}-\text{Al}_2\text{O}_3-\text{GeO}_2-\text{SiO}_2-\text{P}_2\text{O}_5$ Glasses for All-Solid State Batteries

Svetlana V. Pershina *, Tamara A. Kuznetsova, Emma G. Vovkotrub, Semyon A. Belyakov 
and Elena S. Kuznetsova

Institute of High Temperature Electrochemistry of the Ural Branch of the RAS, 20 Akademicheskaya St., Ekaterinburg 620990, Russia

* Correspondence: svpershina_86@mail.ru; Tel.: +7-343-362-31-81; Fax: +7-343-374-59-92

Abstract: Rechargeable Li-metal/Li-ion all-solid-state batteries due to their high safety levels and high energy densities are in great demand for different applications ranging from portable electronic devices to energy storage systems, especially for the production of electric vehicles. The $\text{Li}_{1.5}\text{Al}_{0.5}\text{Ge}_{1.5}(\text{PO}_4)_3$ (LAGP) solid electrolyte remains highly attractive because of its high ionic conductivity at room temperature, and thermal stability and chemical compatibility with electrode materials. The possibility of LAGP production by the glass-ceramic method makes it possible to achieve higher total lithium-ion conductivity and a compact microstructure of the electrolyte membrane compared to the ceramic one. Therefore, the crystallization kinetics investigations of the initial glass are of great practical importance. The present study is devoted to the parent glasses for the production of $\text{Li}_{1.5+x}\text{Al}_{0.5}\text{Ge}_{1.5}\text{Si}_x\text{P}_{3-x}\text{O}_{12}$ glass-ceramics. The glass transition temperature T_g is determined by DSC and dilatometry. It is found that T_g decreases from 523.4 ($x = 0$) to 460 °C ($x = 0.5$). The thermal stability of glasses increases from 111.1 ($x = 0$) to 188.9 °C ($x = 0.3$). The crystallization activation energy of Si-doped glasses calculated by the Kissinger model is lower compared to that of Si-free glasses, so glass-ceramics can be produced at lower temperatures. The conductivity of the glasses increases with the growth of x content.

Keywords: all-solid-state batteries; solid electrolyte membrane; glasses; glass-ceramics; crystallization kinetics; $\text{Li}_{1.5}\text{Al}_{0.5}\text{Ge}_{1.5}(\text{PO}_4)_3$



Citation: Pershina, S.V.; Kuznetsova, T.A.; Vovkotrub, E.G.; Belyakov, S.A.; Kuznetsova, E.S. Solid Electrolyte Membranes Based on $\text{Li}_2\text{O}-\text{Al}_2\text{O}_3-\text{GeO}_2-\text{SiO}_2-\text{P}_2\text{O}_5$ Glasses for All-Solid State Batteries. *Membranes* **2022**, *12*, 1245. <https://doi.org/10.3390/membranes12121245>

Academic Editor: Giovanni Battista Appetecchi

Received: 10 November 2022

Accepted: 5 December 2022

Published: 8 December 2022

Publisher's Note: MDPI stays neutral with regard to jurisdictional claims in published maps and institutional affiliations.



Copyright: © 2022 by the authors. Licensee MDPI, Basel, Switzerland. This article is an open access article distributed under the terms and conditions of the Creative Commons Attribution (CC BY) license (<https://creativecommons.org/licenses/by/4.0/>).

1. Introduction

Lithium-ion batteries are in demand in all spheres of human activity, from portable electronics to electric vehicles and spacecraft due to their high safety levels and high energy density [1–3]. Commercially produced lithium-ion batteries present an inherent hazard of liquid electrolyte leakage, and, when damaged, they are prone to swelling due to changes in temperature. Switching from liquid electrolytes to solid electrolyte membranes can decide the safety issues of lithium-ion power sources [3,4].

Among the numerous classes of oxide conductors reported in recent years, lithium-conducting glasses and glass-ceramics are the most promising solid electrolytes for all-solid-state batteries [2,5–7]. Moreover, similar glass-forming systems have a wider application both in optical materials and in nuclear technologies [8,9]. The $\text{Li}_2\text{O}-\text{Al}_2\text{O}_3-\text{GeO}_2-\text{P}_2\text{O}_5$ glass-forming system is of particular interest since it can be used as a basis for producing NASICON-structured glass-ceramic electrolytes of the $\text{Li}_{1+x}\text{Al}_x\text{Ge}_{2-x}(\text{PO}_4)_3$ series, which have a high conductivity ($10^{-4} \text{ S cm}^{-1}$ at room temperature (RT)), thermal stability, compact microstructure, and chemical compatibility with electrode materials [7,10,11]. All-solid-state batteries with $\text{Li}_{1.5}\text{Al}_{0.5}\text{Ge}_{1.5}(\text{PO}_4)_3$ (or LAGP) solid electrolyte (LiFePO₄ cathode and Li anode) demonstrate a cycling capacity of 131.3 mAh g⁻¹ after 1000 cycles and a high rate cycling stability of 75 mAh g⁻¹ at 5 C, 50 °C [12].

It should be pointed out that the electrical properties of glass-ceramics are considerably dependent on the chemical composition and thermal history [11,13,14]. Thus, the conductivity of lithium-germanium-phosphate glass-ceramics increases with an increase in Al_2O_3 content from $2.25 \cdot 10^{-8} \text{ S cm}^{-1}$ ($\text{LiGe}_2(\text{PO}_4)_3$ composition) to $5.03 \cdot 10^{-4} \text{ S cm}^{-1}$ (LAGP) at 25°C [11]. In [14], the effect of the microstructure of the crystallized LAGP glass on the conductivity is discussed. Controlled glass crystallization result in the glass-ceramics with a homogenous microstructure, which leads to higher conductivity compared to ceramics of the same composition. In [15], the effect of the crystallization temperature on the conductivity of LAGP was studied, which increased from $1.61 \cdot 10^{-3} \text{ S cm}^{-1}$ to $2.91 \cdot 10^{-3} \text{ S cm}^{-1}$ at heat treatment temperatures of 750 and 800°C , respectively. It has been found that to obtain highly conductive LAGP glass-ceramics with the dense microstructure, heat treatment is required at temperatures significantly higher than the crystallization peak temperature, since the activation energy for crystallization (E_c) is quite high ($\sim 400 \text{ kJ mol}^{-1}$) [10,11,16]. Crystallization kinetics is often studied using a non-isothermal model [17,18]. It has been established that doping $\text{Li}_2\text{O-GeO}_2\text{-P}_2\text{O}_5$ glass with Al_2O_3 leads to decrease in E_c from 328 to 300 kJ mol^{-1} [10]. The E_c of $20\text{Li}_2\text{O-6Al}_2\text{O}_3\text{-35GeO}_2\text{-38P}_2\text{O}_5$ glass is reported to be 442 kJ mol^{-1} [19]. Previously, we demonstrated that Al_2O_3 facilitates the processes of glass crystallization and that E_c obtained by the Kissinger model decreases from 435 to 400 kJ mol^{-1} for $12.5\text{Li}_2\text{O-50GeO}_2\text{-37.5P}_2\text{O}_5$ and $20.63\text{Li}_2\text{O-8.12Al}_2\text{O}_3\text{-33.75GeO}_2\text{-37.50P}_2\text{O}_5$ glasses, respectively [16]. It has also been found that both the glass transition temperature and the crystallization temperature decrease with the introduction of alumina. In addition, the lithium-ion conductivity was increased by 18 times compared to undoped glass.

Doping of LAGP glass with SiO_2 reduces E_c down to 264 kJ mol^{-1} [20] or $199 \pm 22 \text{ kJ mol}^{-1}$ for $\text{Li}_{1.5}\text{Al}_{0.5}\text{Ge}_{1.5}\text{P}_{2.5}\text{Si}_{0.5}\text{O}_{12}$ glass [21], while the lithium-ion conductivity of the glass-ceramics crystallized at 750°C is $2.45 \cdot 10^{-4} \text{ S cm}^{-1}$ at RT [22]. Partial substitution of P^{5+} ions by Si^{4+} should result in the formation of sites for Li^+ ions, which is expected to improve the electrical properties of NASICON-structured glass-ceramics. However, systematic studies of the thermal and structural properties of glasses in the $\text{Li}_2\text{O-Al}_2\text{O}_3\text{-GeO}_2\text{-SiO}_2\text{-P}_2\text{O}_5$ system for further production of $\text{Li}_{1.5+x}\text{Al}_{0.5}\text{Ge}_{1.5}\text{Si}_x\text{P}_{3-x}\text{O}_{12}$ glass-ceramics have not yet been carried out.

In this paper, we report the effects of $\text{P}_2\text{O}_5/\text{SiO}_2$ substitution on the thermal, electrical, and structural properties of $\text{Li}_2\text{O-Al}_2\text{O}_3\text{-GeO}_2\text{-P}_2\text{O}_5$ glasses for the creation of a promising solid electrolyte membrane for all-solid state batteries.

2. Experimental

Bulk glass samples of the $\text{Li}_{1.5+x}\text{Al}_{0.5}\text{Ge}_{1.5}\text{Si}_x\text{P}_{3-x}\text{O}_{12}$ ($x = 0, 0.1, 0.2, 0.3, 0.4, 0.5$) series were prepared by the standard melt quenching method using Li_2CO_3 ($>99.4\%$, Reakhim, Moscow, Russia), Al_2O_3 ($>99.9\%$, Reakhim, Moscow, Russia), GeO_2 ($>99.9\%$, Reakhim, Moscow, Russia), SiO_2 ($>98.0\%$, Reakhim, Moscow, Russia), and $\text{NH}_4\text{H}_2\text{PO}_4$ ($\geq 98.0\%$, Reakhim, Moscow, Russia). Table 1 shows the compositions of $\text{Li}_{1.5+x}\text{Al}_{0.5}\text{Ge}_{1.5}\text{Si}_x\text{P}_{3-x}\text{O}_{12}$ glass samples. The starting components were thoroughly mixed together. The charge was heated stepwise up to 500°C with exposure at the final temperature for 2 h to remove volatile components. The resulting mixture was melted in a Pt crucible at 1250°C for 1 h in air. To obtain glasses, the melt was quenched between preheated steel plates with cooling rate $\sim 10^2 \text{ }^\circ\text{C min}^{-1}$. Then all obtained samples were annealed at $420\text{--}500^\circ\text{C}$ for 2 h depending on the composition and cooled slowly to RT in a furnace at a rate of 1°C min^{-1} . As a result, transparent colorless parallel-sided plates without any impurities were obtained.

Table 1. Compositions of $\text{Li}_{1.5+x}\text{Al}_{0.5}\text{Ge}_{1.5}\text{Si}_x\text{P}_{3-x}\text{O}_{12}$ glasses in mole percent and sample density (ρ).

Glass Code	x Value	Method	Li_2O , mol%	Al_2O_3 , mol%	GeO_2 , mol%	SiO_2 , mol%	P_2O_5 , mol%	(Li+Al)/(Ge+Si+P)	O/P	$\rho \pm 0.04$, g cm^{-3}
0Si	0.0	nominal	18.75	6.25	37.50	–	37.50	0.33	4.1	2.98
		AES	18.0	7.0	38.1	–	36.9			
0.1Si	0.1	nominal	19.51	6.09	36.59	2.44	35.37	0.34	4.2	3.03
		AES	18.9	6.9	37.0	2.5	34.7			
0.2Si	0.2	nominal	20.24	5.95	35.71	4.76	33.34	0.35	4.3	3.01
		AES	20.1	6.0	36.2	4.6	33.1			
0.3Si	0.3	nominal	20.93	5.81	34.88	6.98	31.40	0.36	4.5	3.05
		AES	20.8	5.9	35.3	7.1	30.9			
0.4Si	0.4	nominal	21.59	5.68	34.09	9.09	29.55	0.36	4.6	2.96
		AES	20.9	5.6	34.3	9.0	30.2			
0.5Si	0.5	nominal	22.22	5.56	33.33	11.11	27.78	0.38	4.7	2.87
		AES	22.0	5.6	33.0	11.1	28.3			

The amorphous structure of the obtained glasses and the crystalline phases present after heat treatment were determined by X-ray diffraction method (XRD) on a Rigaku D/MAX-2200VL/PC diffractometer (Rigaku Corporation, Tokyo, Japan) using $\text{Cu K}\alpha$ radiation in the range of $10 \leq 2\theta \leq 80$ at RT.

The chemical composition of the glasses was determined by atomic emission spectroscopy (AES) with inductively coupled plasma using an Optima 4300 DV (PerkinElmer, Waltham, MA, USA) spectrometer. The measurement accuracy was 2–3%.

The glass transition temperature (T_g), crystallization onset temperature (T_c), and crystallization peak temperature (T_p) were established by differential scanning calorimetry (DSC) on a thermal analyzer Netzsch STA 449 F1 Jupiter (NETZSCH-Gerätebau GmbH, Selb, Germany) at the rate of 3, 5, 10, 15, and 25 $^\circ\text{C min}^{-1}$ in Pt crucibles in the 35–750 $^\circ\text{C}$ temperature range in air (20 mL min^{-1}).

Linear thermal expansion was investigated on the samples in the form of rectangular glass bars in a push-rod quartz dilatometer. The measurements were performed by Tesatronic TT80 (TESA, Urdorf, Switzerland) digital meter with a high-precision TESA GT 21HP probe (a sensitivity of 0.01 μm) in the temperature range of 25–600 $^\circ\text{C}$ at a heating rate of 3 $^\circ\text{C min}^{-1}$.

The density of the samples was estimated by Archimedes principle at 25 $^\circ\text{C}$ in several parallels.

The electrical resistance of the samples was measured by the electrochemical impedance method in a two-probe cell with silver metal electrodes in air. An Ellins P-5X potentiostat/galvanostat (Elins, Chernogolovka, Russia) was used for resistance measurement. For this measurement, the samples were polished and coated with Ga-Ag paste to form the electrodes. The impedance spectra were obtained in the frequency range of 0.025–1000 kHz and the temperature range of 150–300 $^\circ\text{C}$.

Raman spectra were recorded at RT on a Renishaw Ramascope U1000 equipped with a confocal Leica DML microscope (Renishaw, New Mills, UK) operating on a solid-state laser ($\lambda = 532$ nm) with a power of 5 mW on the sample. Spectral calibration was performed using the Raman spectrum of silica. The spectral resolution was 1 cm^{-1} . The intensities were normalized to the maximum value.

Infrared spectra were obtained using a Fourier-transform infrared spectrophotometer (FT-IR) Tensor 27 Bruker (Bruker Optik GmbH, Ettlingen, Germany) and KBr pellet technique. IR spectra were recorded in the wavenumber range 400–4000 cm^{-1} with a spectral

resolution of 0.9 cm^{-1} with 32-fold scanning. Sample powders were mixed with KBr (1:200) and pressed to get a transparent pellet.

3. Results and Discussion

3.1. Characterization and Thermal Behavior of the Glasses

Figure 1 shows powder diffraction patterns of compositions based on the $\text{Li}_2\text{O}-\text{Al}_2\text{O}_3-\text{GeO}_2-\text{SiO}_2-\text{P}_2\text{O}_5$ system with different additive contents. It can be seen from the XRD data that all samples show haloes characteristic of amorphous materials without peaks of crystalline phases.

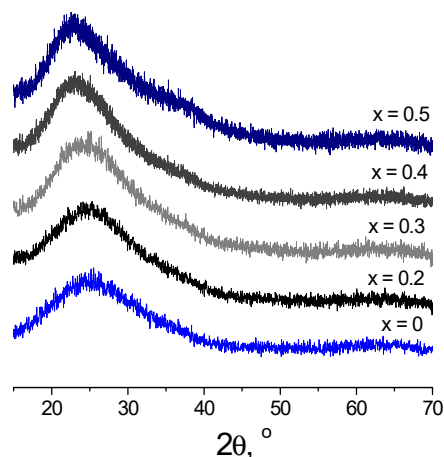


Figure 1. XRD patterns of $\text{Li}_{1.5+x}\text{Al}_{0.5}\text{Ge}_{1.5}\text{Si}_x\text{P}_{3-x}\text{O}_{12}$ glasses.

DSC analysis at different heating rates ($3, 5, 10, 15,$ and $25 \text{ }^\circ\text{C min}^{-1}$) was performed to understand the crystallization kinetics and thermal stability of glasses. Figure 2 shows the DSC-curves of 0.1Si glass at $10 \text{ }^\circ\text{C min}^{-1}$. Bends around $500\text{--}530 \text{ }^\circ\text{C}$ depending on the heating rate for 0.1Si glass are related to the glass transition temperature (T_g), while exothermic reactions indicate the crystallization process. As can be seen, T_g increases from $505 \text{ }^\circ\text{C}$ to $523.4 \text{ }^\circ\text{C}$ with an increase in the heating rate from 3 to $25 \text{ }^\circ\text{C min}^{-1}$ (Figures 2 and 3a). On the DSC curves of SiO_2 -contained glasses at a heating rate of $10 \text{ }^\circ\text{C min}^{-1}$, T_g decreases gradually from 523.4 to $460.0 \text{ }^\circ\text{C}$ with increasing x from 0 to 0.5 (Figure 3d). This is probably due to the substitution of P-O bonds (589 kJ mol^{-1}) [23] by Si-O bonds (452 kJ mol^{-1}) [24] with a lower bond enthalpy.

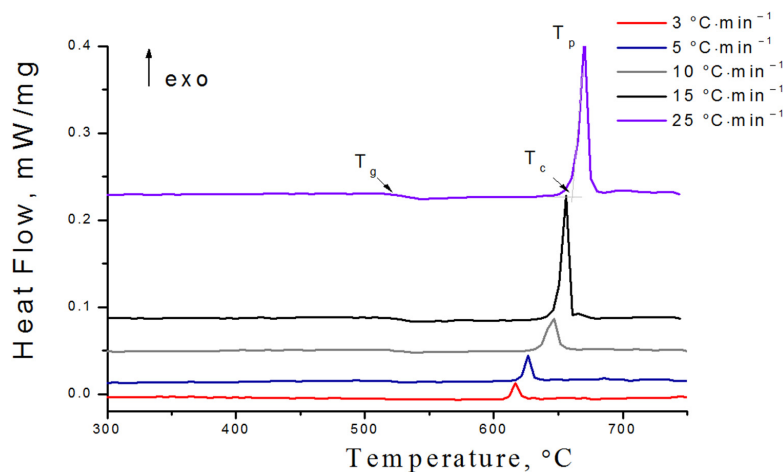


Figure 2. DSC curves of bulk 0.1Si glass at different heating rates.

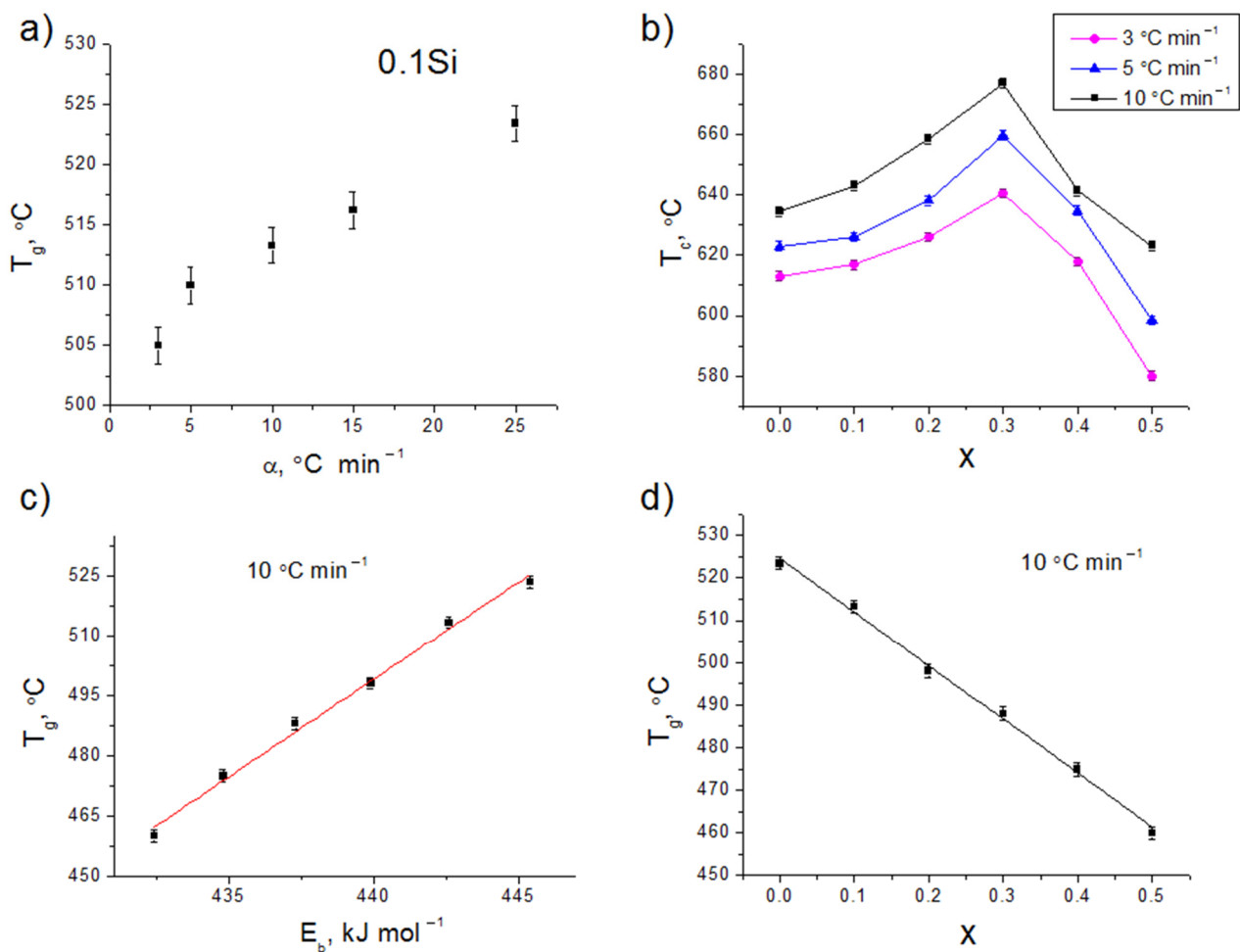


Figure 3. Characteristic temperatures: the glass transition temperatures (T_g) of the cast 0.1Si glass (a) and the crystallization peak onset temperatures (T_c) of $\text{Li}_{1.5+x}\text{Al}_{0.5}\text{Ge}_{1.5}\text{Si}_x\text{P}_{3-x}\text{O}_{12}$ glasses at different heating rates (b) and at the rate of 10 °C min⁻¹ (c,d).

The values of T_g correlated with the average single bond enthalpy (E_B) of glasses (Figure 3c), which was calculated as:

$$E_B = \frac{x \cdot E_{\text{Li-O}} + y \cdot E_{\text{Al-O}} + z \cdot E_{\text{Ge-O}} + a \cdot E_{\text{Si-O}} + b \cdot E_{\text{P-O}}}{100} \quad (1)$$

where x , y , z , a , b are the content of the corresponding oxides in mol%; $E_{\text{Li-O}}$, $E_{\text{Al-O}}$, $E_{\text{Ge-O}}$, and $E_{\text{P-O}}$ are single bond dissociation energies for Li–O (341 kJ mol⁻¹) [25], Al–O (512 kJ mol⁻¹) [25], Ge–O (343 kJ mol⁻¹) [26], Si–O (452 kJ mol⁻¹) [24], and P–O (589 kJ mol⁻¹) [23], respectively.

Figure 3c shows the change in T_g depending on the E_B of the compositions. As can be seen, T_g increases with increasing E_B . Similar dependences were also obtained for other oxide glasses [25]. It is well-known that T_g depends on the cross-link density and closeness of the packing of the glass [27–29], which will be considered in Section 3.4. Another reason for these changes in T_g is probably in reducing the glass network connectivity as the $\text{SiO}_2/\text{P}_2\text{O}_5$ ratio increases. It is noteworthy that an increase in the x content is accompanied by the increase in the ratio of the dopants ($\text{Li}_2\text{O} + \text{Al}_2\text{O}_3$) to the glass formers ($\text{GeO}_2 + \text{SiO}_2 + \text{P}_2\text{O}_5$) in the studied series of glasses (Table 1). Modifiers destroy the chains in the glass network, causing a decrease in T_g with increasing x (Figure 3d).

In addition, the glass transition point (T_g) was determined by push-rod quartz dilatometry to compare the results with DSC data. The glass transformation temperature was

determined from the change in the slope of the elongation versus temperature plot (Figure 4). The T_g from thermal expansion was found to be 520 °C compared to 519.7 °C for 0Si glass at the same heating rate (3 °C min⁻¹). Figure 4 shows that T_g decreases while the thermal expansion coefficient increases with the additive content.

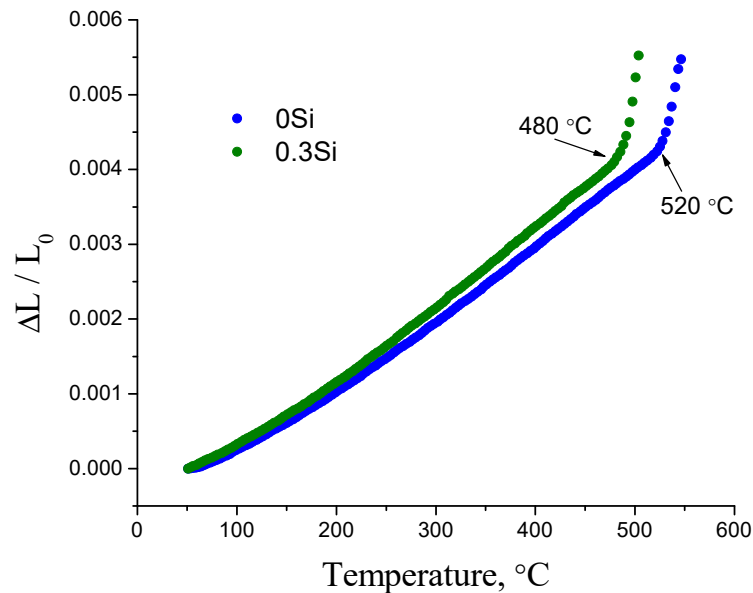


Figure 4. Thermal expansion dependences of 0Si and 0.3Si glasses.

3.2. Crystallization Behavior

The crystallization peak onset temperatures (T_c) and the crystallization peak temperatures (T_p) shift toward higher values (Figure 3b, Table 2) as the heating rate increases. A similar behavior is also characteristic of other glassy systems [30]. An increase in x is accompanied by a gradual increase in T_c from 623 °C ($x = 0$) to 659.7 °C ($x = 0.3$) followed by a considerable decrease to 598.5 °C ($x = 0.5$) at a constant heating rate (5 °C min⁻¹), which should be related to structural changes in the glass network.

The thermal stability of glasses was determined as $\Delta T = T_c - T_g$ and is given in Table 2 for different heating rates. It has been established that ΔT increases from 111.1 °C ($x = 0$) to 188.9 °C ($x = 0.3$), and then decreases to 163 °C ($x = 0.5$) at the rate of 10 °C min⁻¹. An extremum in the plot of thermal stability vs. concentration at $x = 0.3$ is observed for all heating rates. An increase in the thermal stability of the glasses up to $x = 0.3$ indicates an increase in the glass formation temperature range to obtain the desired membrane geometry.

The activation energy for crystallization (E_c) of glasses is an important parameter in the analysis of the crystallization process of glasses for the glass-ceramics production. E_c was calculated by the Kissinger equation:

$$\ln\left(\frac{\alpha}{T_p^2}\right) = \left(-\frac{E_c}{RT_p}\right) + const \tag{2}$$

where R is the ideal gas constant and α is the heating rate.

Figure 5 shows plots of the dependence $\ln\left(\frac{\alpha}{T_p^2}\right)$ versus $1/T_p$ for the glasses obtained. The E_c calculated from the slope of the linear curve shown in Figure 5 is 400 kJ mol⁻¹ for 0Si glass (Li_{1.5}Al_{0.5}Ge_{1.5}(PO₄)₃ composition) and is in good agreement with the data of [16,31], confirming the correctness of our data. E_c initially decreases with increasing x content and reaches a minimum at $x = 0.4$ (Figure 6). A similar trend in E_c with SiO₂ doping was obtained in [20,21]. The introduction of SiO₂ was found to decrease E_c down to 128 kJ mol⁻¹; therefore, less energy is required for incorporating crystals into the Li₂O–Al₂O₃–GeO₂–

SiO₂-P₂O₅ glass matrix. Hence, a Si-containing glass-ceramic membrane can be obtained at temperatures below 820 °C, which is optimal for obtaining Li_{1.5}Al_{0.5}Ge_{1.5}(PO₄)₃ solid electrolyte [11].

Table 2. The values of characteristic temperature of Li_{1.5+x}Al_{0.5}Ge_{1.5}Si_xP_{3-x}O₁₂ glasses: glass transition temperatures (*T_g*), crystallization peak onset temperatures (*T_c*), crystallization peak temperatures (*T_p*) and thermal stability (ΔT) at different heating rates (α). The measurement accuracy of the characteristic temperatures was ± 1.5 °C.

x	α , °C min ⁻¹	<i>T_g</i> , °C	<i>T_c</i> , °C	<i>T_p</i> , °C	ΔT , °C
0	3	519.7	613	616.9	93.3
	5	523	623	625.4	100
	10	523.4	634.5	636.0	111.1
0.1	3	505	616.9	619.6	111.9
	5	510	626.1	629.9	116.1
	10	513.3	642.9	646.6	129.6
	15	527.6	652.9	657.8	125.3
	25	523.4	665.2	672.8	141.8
0.2	3	495.6	626	632.1	130.4
	5	498.4	638.1	645.3	139.7
	10	498	658.5	667.9	160.5
0.3	3	472	640.5	646	168.5
	5	485.1	659.7	667.1	174.6
	10	488	676.9	701.9	188.9
0.4	3	458.7	617.8	631.9	159.1
	5	475.7	634.8	655	159.1
	10	474.9	641.2	692.5	166.3
0.5	3	440	580	631.2	140
	5	462	598.5	653.7	136.5
	10	460	623	683.8	163

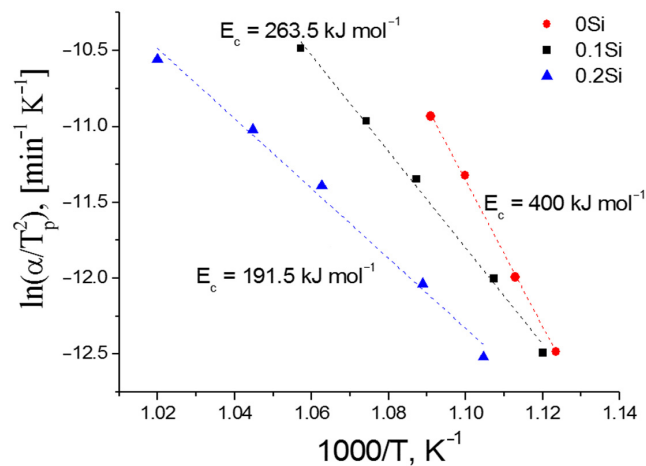


Figure 5. Kissinger plots of $\ln\left(\frac{\alpha}{T_p^2}\right)$ versus $1/T_p$ for 0Si–0.2Si glasses.

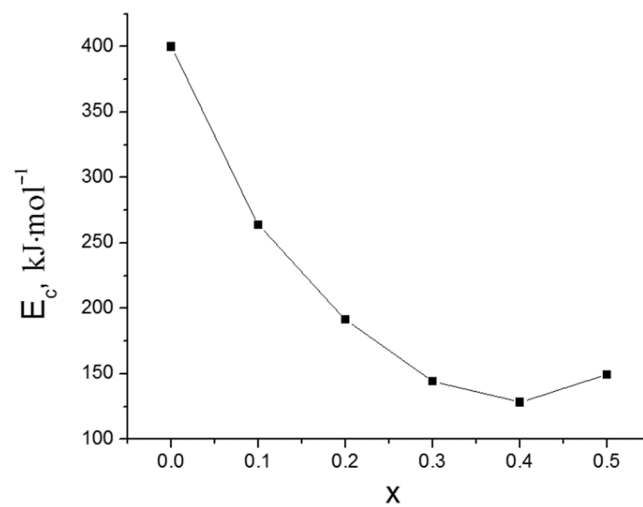


Figure 6. Crystallization activation energy of $\text{Li}_{1.5+x}\text{Al}_{0.5}\text{Ge}_{1.5}\text{Si}_x\text{P}_{3-x}\text{O}_{12}$ glasses as a function of x .

The phase composition of the glass-ceramic samples after heat treatment at 820 °C for 2 h was determined. According to XRD data, $\text{LiGe}_2(\text{PO}_4)_3$ with a NASICON-type structure is formed together with the impurity phases of AlPO_4 , $\text{Li}_4\text{P}_2\text{O}_7$, SiO_2 , and $\text{Li}_9\text{Al}_3(\text{P}_2\text{O}_7)_3(\text{PO}_4)_2$, which appear at $x > 0.1$.

3.3. Transport Properties of Glasses

Figure 7 shows typical impedance spectra of the glasses obtained. The impedance spectra have a shape characteristic of ion-conducting glasses and are fitted according to the equivalent circuit (Figure 7 inset). A similar equivalent circuit was applied in the works [32,33]. The high-frequency semicircle corresponds to bulk response (R) and the low frequency tail characterized the electrode polarization (an additional constant phase element CPE2) [16,34]. It should be noted that the formation of a single arc emerging from the origin is typical for single-phase systems. An increase in the additive content leads to a decrease in the resistance.

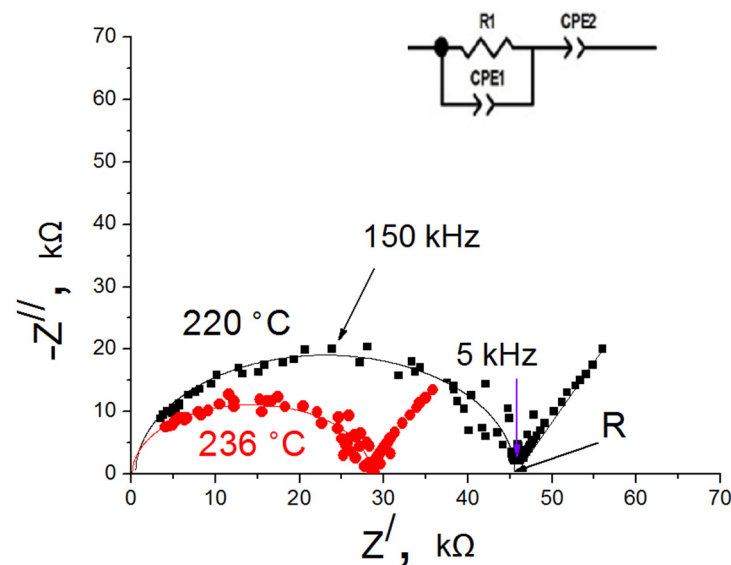


Figure 7. Impedance spectra of 0.3Si glass at 220 °C (black) and 236 °C (red).

Taking into account the fitted values of the resistance according to the equivalent circuit and the geometry of the samples, the specific conductivity of the glasses (σ) was calculated at different temperatures (Figure 8a). It has been found that the conductivity

of all compositions demonstrates an Arrhenius temperature dependence, which indicates the absence of phase transitions in the temperature range studied and agrees with the DSC data. According to the Arrhenius equation [16], the activation energy for conduction (E_a) was calculated from the temperature dependences of conductivity. E_a decreases from $80.4 \pm 0.5 \text{ kJ mol}^{-1}$ ($0.83 \pm 0.01 \text{ eV}$) to 71.5 ± 0.9 ($0.74 \pm 0.01 \text{ eV}$) kJ mol^{-1} for $x = 0$ and $x = 0.5$, respectively, as the conductivity increases (Figure 8b). The electrical conductivity of the parent glasses for glass-ceramics production at room temperature is $<10^{-10} \text{ S}\cdot\text{cm}^{-1}$, however, heat treatment of these glasses under optimal conditions increased the conductivity by several orders of magnitude up to $\sim 10^{-4} \text{ S}\cdot\text{cm}^{-1}$ (Figures 8b and 9).

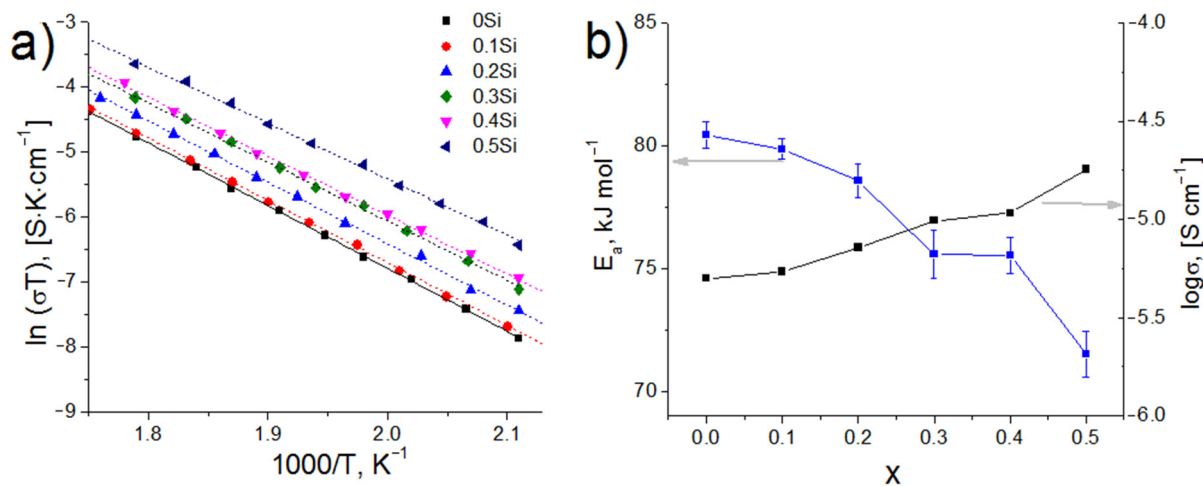


Figure 8. Arrhenius plots of the conductivity for 0Si-0.5Si glasses (a) and composition dependences of the E_a (blue) and conductivity (black) of $\text{Li}_{1.5+x}\text{Al}_{0.5}\text{Ge}_{1.5}\text{Si}_x\text{P}_{3-x}\text{O}_{12}$ glasses at $250 \text{ }^\circ\text{C}$ (b).

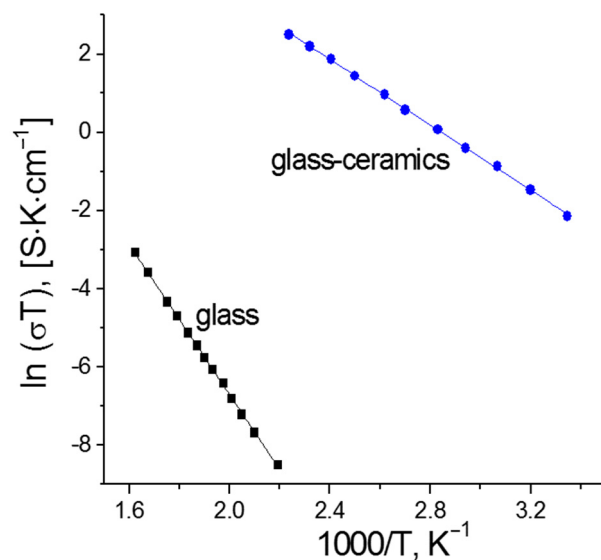


Figure 9. Comparison of total conductivity for $\text{Li}_{1.6}\text{Al}_{0.5}\text{Ge}_{1.5}\text{Si}_{0.1}\text{P}_{2.9}\text{O}_{12}$ glass and glass-ceramics.

3.4. Short-Range Structure of the Glasses

The changes in the crystallization behavior, thermal and transport properties of the glasses investigated due to short-range structural changes were studied by Raman and IR spectroscopy. Figure 10 shows the evolution of the Raman spectra with x content.

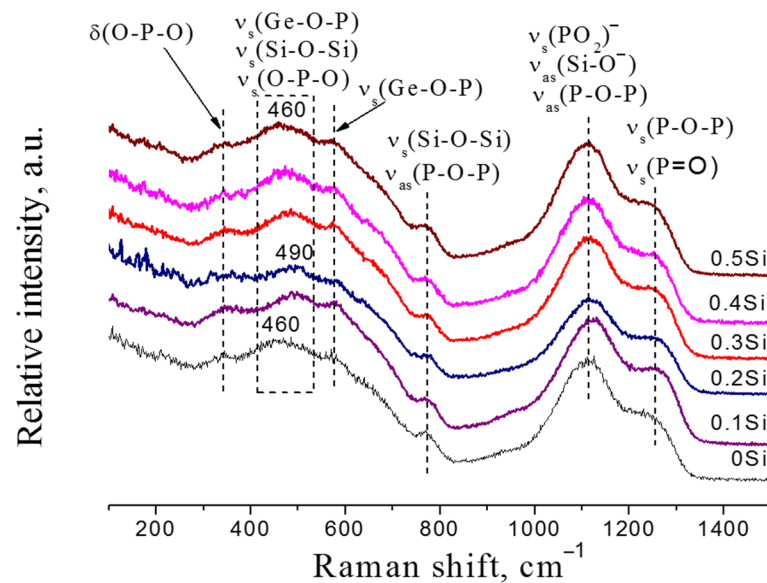


Figure 10. Raman spectra for 0Si–0.5Si glasses at room temperature.

The multicomponent glasses under study contain PO_4 , GeO_4 , and SiO_4 tetrahedra, which form various types of connections between themselves and groups with bridging and non-bridging oxygen atoms. At the stoichiometric ratio $\text{O}/\text{P} = 4$, orthophosphate groups (Q^1) should prevail in the glass network, which was pointed out in [35].

The Raman bands near $600\text{--}1400\text{ cm}^{-1}$ are due to phosphate units, and the bands at $400\text{--}1000\text{ cm}^{-1}$ range are due to germanate units introduced into phosphate chains. The correlation of bands with vibration modes is given in Table 3. The shoulder around 1255 cm^{-1} is related to the $\text{P}=\text{O}$ vibrations [36–38] and the symmetric stretching vibrations of the P-O-P bond [39]. The peak at 1115 cm^{-1} is associated with the asymmetric stretching vibrations of the P-O-P bond [39,40] and symmetric stretching vibrations of the Q^2 phosphate tetrahedra [36–39]. In addition, this band indicates the formation of non-bridging oxygen associated with $\text{Q}^3\text{ SiO}_4$ tetrahedra [40–42]. The band at 775 cm^{-1} is due to the symmetric and asymmetric stretching vibrations of the P-O-P bond [37–40,42] and symmetric stretching vibrations of the Si-O-Si bond [42,43]. The bands around 460 and 575 cm^{-1} are related to symmetric stretching vibrations of the Ge-O-P bond [11] and also the vibrations of the phosphate and silicate tetrahedra [42,44], respectively. With increasing x content, the most intense band at 460 cm^{-1} shifts to 490 cm^{-1} for $x = 0$ and $x = 0.2$, respectively. Then the band at 490 cm^{-1} moves to 460 cm^{-1} up to $x = 0.5$, while some bands remain unchanged. This should be due to the destruction of Ge-O-P bonds and the appearance of new Ge-O-Si or Ge-O-Ge bonds [11,45,46]. The Raman spectra are difficult to interpret due to the overlap of the bands related to phosphate and silicate units. Additional information about the molecular structure of the glasses under study was obtained using IR-spectroscopy.

The IR-spectra of undoped and SiO_2 -doped glasses are shown in Figure 10. All IR-spectra consist of five relatively broad bands, which indicate a strong modification of the glass network [16]. The bands appearing in the $1100\text{--}1200\text{ cm}^{-1}$ region are associated with the vibrations of terminal (Q^1) phosphate tetrahedra, namely the O-P-O asymmetric stretching vibrations [16,47,48] and asymmetric stretching vibrations of the P-O^- bond [36,37,49]. The shoulder at around 950 cm^{-1} results from the asymmetric stretching vibrations of both P-O-P and Ge-O-Ge bonds [16,50–52]. The band centered at 775 cm^{-1} is due to symmetric Ge-O-P or P-O-P stretching vibrations [16,50,52]. The shoulder around 1260 cm^{-1} , related to the $\text{P}=\text{O}$ vibrations [50,53], is very weak because stronger P-O-Ge or P-O-Si bonds are formed.

Table 3. Assignments of various vibrational bands from Raman spectra of the glasses obtained.

Band Position, cm^{-1}	Band Assignments	References
1255	ν_s (P–O–P) ν_s (P=O)	[39] [36–38]
1115	ν_s (PO_2) [−] ν_{as} (P–O–P) ν_{as} (Si–O [−])	[36–39] [39,40] [40–42]
775	ν_{as} (P–O–P) ν_s (P–O–P) ν_s (Si–O–Si)	[38–40] [37,42] [42,43]
575	ν_s (O–Si–O) ν_s (O–P–O) ν_s (Ge–O–P)	[42,44] [42] [11]
460–490	ν_s (O–P–O) ν_s (Ge–O–Ge)	[41,42] [11,45,46]
340	δ (O–P–O)	[37]

As the x content increases, several main features are observed: (i) the band at 958 cm^{-1} ($x = 0$) shifts to 940 cm^{-1} ($x = 0.5$), (ii) the intensity of the band at 775 cm^{-1} becomes smaller up to $x = 0.4$, (iii) the 510 cm^{-1} band moves toward a lower wavenumber reaching 490 cm^{-1} in the spectrum of $x = 0.2$, and then shifts to 507 cm^{-1} for $x = 0.5$. These changes indicate the gradual depolymerization of the phosphate network with the formation of a mixed complex silicon-phosphate-germanate glass network, which results in a decrease in the density of the samples (Table 1). The loosening of the glass network is due to the growing number of the modifiers ($\text{Li}_2\text{O} + \text{Al}_2\text{O}_3$) and the decrease in the number of the glass-formers ($\text{GeO}_2 + \text{SiO}_2 + \text{P}_2\text{O}_5$).

The decrease of T_g and the increase of the thermal expansion coefficient may be related to the loosening of the glass network, i.e., to the growing number of Q¹ phosphate units. As can be seen from Figure 11, the IR-spectra of 0Si and 0.1Si compositions, as well as those for 0.3Si and 0.4Si compositions, have a similar appearance and, as can be seen from Figure 8a,b, their conductivity values are close. The growth of lithium-ion conductivity of SiO₂-doped glasses is due to two factors: an increase in the number of non-bridging oxygen atoms, which are sites for the migration of Li⁺ ions, and the increase in the concentration of charge carriers (Li⁺).

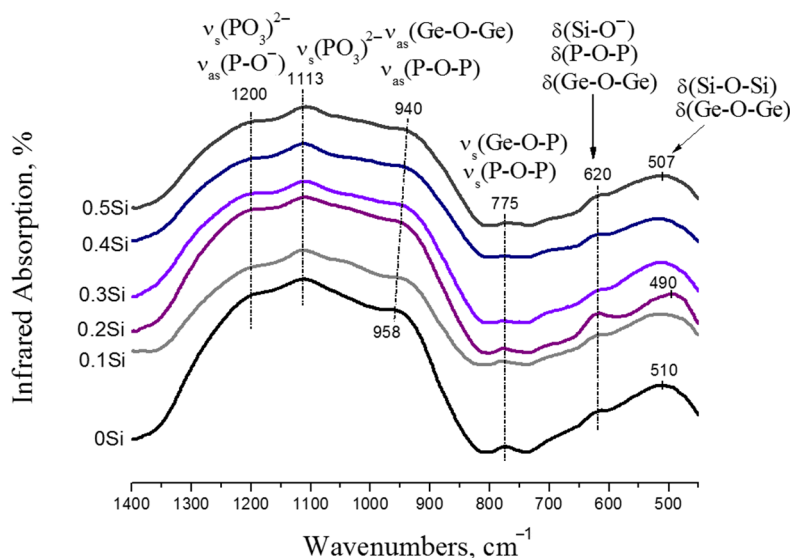


Figure 11. FT-IR spectra of 0Si–0.5Si glasses.

4. Conclusions

The effect of P_2O_5/SiO_2 substitution on the $Li_2O-Al_2O_3-GeO_2-P_2O_5$ glasses examined by DSC shows that T_g decreases from 523.4 to 460 °C as the x content increases from 0 to 0.5, respectively, due to the substitution of P–O bonds (589 kJ mol^{−1}) for Si–O (452 kJ mol^{−1}) with the lower bond enthalpy. The change in T_g is consistent with the results of dilatometry. A correlation between T_g and E_B was established. It was found that the thermal stability of glasses increases up to $x = 0.3$, which indicates the increase in the temperature range for the formation of SiO_2 -containing glasses in order to obtain the desired membrane geometry. The activation energy of glass crystallization significantly decreases from 400 to 128 kJ mol^{−1} for $x = 0$ and $x = 0.4$, respectively. Thus, the Si-containing glass-ceramic membrane can be obtained at temperatures below 820 °C, which is optimal for obtaining SiO_2 -undoped glass-ceramics. The Li^+ conductivity of the glasses increases as a function of x . The changes in the thermal and electrical properties with the change in the content of x are related to short-range structural changes in the glasses. The infrared spectra show the formation of the Q^1 phosphate groups as x increases. The results of structural studies demonstrate the gradual depolymerization of the phosphate network. So, the decrease in the connectivity of the glass network, which accompanies the increase in SiO_2/P_2O_5 ratio, is the reason for the decrease in T_g and the enhancement in conductivity. It should be noted that the conductivity of the glass-ceramics obtained from SiO_2 -doped glasses has high values ($>10^{-4}$ S cm^{−1} at RT). Therefore, they can be considered as promising solid electrolytes for all-solid-state batteries.

Author Contributions: Conceptualization, S.V.P.; validation, S.V.P.; formal analysis, E.S.K.; investigation, S.V.P., T.A.K., E.G.V., S.A.B. and E.S.K.; performing experiments, S.V.P.; data collection, S.V.P.; writing—original draft, S.V.P.; writing—review and editing, S.V.P. and S.A.B.; visualization, S.V.P. and E.S.K.; project administration, S.V.P. All authors have read and agreed to the published version of the manuscript.

Funding: The study reported was funded by the Russian Science Foundation according to the research project No. 22-23-01099.

Institutional Review Board Statement: Not applicable.

Data Availability Statement: Not applicable.

Acknowledgments: The characterization of materials was carried out at the Shared Access Centre “Composition of Compounds”, IHTE UB RAS.

Conflicts of Interest: The authors declare no conflict of interest.

References

1. Zhang, F.; Huang, Q.A.; Tang, Z.; Li, A.; Shao, Q.; Zhang, L.; Li, X. A review of mechanics-related material damages in all-solid-state batteries: Mechanisms, performance impacts and mitigation strategies. *Nano Energy* **2020**, *70*, 104545. [[CrossRef](#)]
2. Zhang, Z.; Shao, Y.; Lotsch, B.; Hu, Y.-S.; Li, H.; Janek, J.; Nazar, L.F.; Nan, C.-W.; Maier, J.; Armand, M.; et al. New horizons for inorganic solid state ion conductors. *Energy Environ. Sci.* **2018**, *11*, 1945–1976. [[CrossRef](#)]
3. Sun, C.; Liu, J.; Gong, Y.; Wilkinson, D.P.; Zhang, J. Recent advances in all-solid-state rechargeable lithium batteries. *Nano Energy* **2017**, *33*, 363–386. [[CrossRef](#)]
4. Liu, Q.; Jiang, L.; Zheng, P.; Sun, J.; Liu, C.; Chai, J.; Li, X.; Zheng, Y.; Liu, Z. Recent Advances in Stability Issues of Inorganic Solid Electrolytes and Composite Solid Electrolytes for All-Solid-State Batteries. *Chem. Rec.* **2022**, *22*, e202200116. [[CrossRef](#)]
5. Wang, Y.; Richards, W.D.; Ong, S.P.; Mara, L.J.; Kim, J.C.; Mo, Y.; Ceder, G. Design principles for solid-state lithium superionic conductors. *Nat. Mater.* **2015**, *14*, 1026–1031. [[CrossRef](#)]
6. Bates, J.B.; Dudney, N.J.; Neudecker, B.; Ueda, A.; Evans, C.D. Thin film lithium and lithium-ion batteries. *Solid State Ion.* **2000**, *135*, 33–45. [[CrossRef](#)]
7. Pershina, S.V.; Il'ina, E.A.; Druzhinin, K.V.; Farlenkov, A.S. Effect of $Li_2O-Al_2O_3-GeO_2-P_2O_5$ glass crystallization on stability versus molten lithium. *J. Non-Cryst. Solids* **2020**, *527*, 119708. [[CrossRef](#)]
8. Klym, H.; Ingram, A.; Shpotyuk, O.; Hotra, O.; Popov, A.I. Positron trapping defects in free-volume investigation of Ge–Ga–S–CsCl glasses. *Radiat. Meas.* **2016**, *90*, 117–121. [[CrossRef](#)]

9. Kozlovskiy, A.; Shlimas, D.I.; Zdorovets, M.V.; Popova, E.; Elsts, E.; Popov, A.I. Investigation of the Efficiency of Shielding Gamma and Electron Radiation Using Glasses Based on $\text{TeO}_2\text{-WO}_3\text{-Bi}_2\text{O}_3\text{-MoO}_3\text{-SiO}_2$ to Protect Electronic Circuits from the Negative Effects of Ionizing Radiation. *Materials* **2022**, *15*, 6071. [[CrossRef](#)]
10. Kun, H.; Yanhang, W.; Chengkui, Z.; Huifeng, Z.; Yonghua, L.; Jiang, C.; Bin, H.; Juanrong, M. Influence of Al_2O_3 additions on crystallization mechanism and conductivity of $\text{Li}_2\text{O-GeO}_2\text{-P}_2\text{O}_5$ glass-ceramics. *Physica B* **2011**, *406*, 3947–3950. [[CrossRef](#)]
11. Pershina, S.V.; Antonov, B.D.; Farlenkov, A.S.; Vovkotrub, E.G. Glass-ceramics in $\text{Li}_{1+x}\text{Al}_x\text{Ge}_{2-x}(\text{PO}_4)_3$ system: The effect of Al_2O_3 addition on microstructure, structure and electrical properties. *J. Alloys Compd.* **2020**, *835*, 155281. [[CrossRef](#)]
12. Jiang, P.; Cao, J.; Wei, B.; Qian, G.; Wang, S.; Shi, Y.; Du, G.; Lu, X.; Ouyang, C.; Cao, F.; et al. LiF involved interphase layer enabling thousand cycles of LAGP-based solid-state Li metal batteries with 80% capacity retention. *Energy Storage Mater.* **2022**, *48*, 145–154. [[CrossRef](#)]
13. Kuo, P.H.; Du, J. Crystallization behavior of $\text{Li}_{1+x}\text{Al}_x\text{Ge}_{2-x}(\text{PO}_4)_3$ glass-ceramics: Effect of composition and thermal treatment. *J. Non-Cryst. Solids* **2019**, *525*, 119680. [[CrossRef](#)]
14. Cruz, A.M.; Ferreira, E.B.; Rodrigues, A.C.M. Controlled crystallization and ionic conductivity of a nanostructured LiAlGePO_4 glass-ceramic. *J. Non-Cryst. Solids* **2009**, *355*, 2295–2301. [[CrossRef](#)]
15. Zhu, Y.; Zhang, Y.; Lu, L. Influence of crystallization temperature on ionic conductivity of lithium aluminum germanium phosphate glass-ceramic. *J. Power Sourc.* **2015**, *290*, 123–129. [[CrossRef](#)]
16. Pershina, S.V. Structural, thermal and electrical properties of $\text{Li}_2\text{O-Al}_2\text{O}_3\text{-GeO}_2\text{-P}_2\text{O}_5$ glasses. *J. Alloys Compd.* **2021**, *871*, 159532. [[CrossRef](#)]
17. Lucci, A.; Battezzati, L.; Antonione, C.; Riontino, G. Influence of preannealing on crystallization kinetics of some metallic glasses. *J. Non-Cryst. Solids* **1981**, *44*, 287–295. [[CrossRef](#)]
18. Prasad, N.S.; Varma, K.B.R. Crystallization kinetics of the $\text{LiBO}_2\text{-Nb}_2\text{O}_5$ glass using differential thermal analysis. *J. Am. Ceram. Soc.* **2005**, *88*, 357–361. [[CrossRef](#)]
19. Kun, H.; Yanhang, W.; Chengkui, Z.; Yonghua, L.; Huifeng, Z.; Bin, H.; Jiang, C. Crystallization Kinetics of Lithium Aluminum Germanium Phosphate Glass by DSC Technique. *J. Wuhan Univ. Technol.-Mater. Sci. Ed.* **2012**, *27*, 63–66. [[CrossRef](#)]
20. Das, A.; Dixit, A.; Goswami, M.; Mythili, R.; Hajra, R.N. Study on crystallization kinetics and phase evolution in $\text{Li}_2\text{O-Al}_2\text{O}_3\text{-GeO}_2\text{-P}_2\text{O}_5$ glass ceramics system. *AIP Conf. Proc.* **2018**, *1942*, 140022. [[CrossRef](#)]
21. Das, A.; Goswami, M.; Krishnan, M. Crystallization kinetics of $\text{Li}_2\text{O-Al}_2\text{O}_3\text{-GeO}_2\text{-P}_2\text{O}_5$ glass-ceramics system. *J. Therm. Anal. Calorim.* **2018**, *131*, 2421–2431. [[CrossRef](#)]
22. Das, A.; Goswami, M.; Krishnan, M. Study on electrical and structural properties in SiO_2 substituted $\text{Li}_2\text{O-Al}_2\text{O}_3\text{-GeO}_2\text{-P}_2\text{O}_5$ glass-ceramic systems. *Ceram. Int.* **2018**, *44*, 13373–13380. [[CrossRef](#)]
23. Kilic, G.; Ilik, E.; Mahmoud, K.A.; El-Agawany, F.I.; Alomairy, S.; Rammah, Y.S. The role of B_2O_3 on the structural, thermal, and radiation protection efficacy of vanadium phosphate glasses. *Appl. Phys. A* **2021**, *127*, 265. [[CrossRef](#)]
24. Dubois, G.; Volksen, W.; Magbitang, T.; Miller, R.D.; Gage, D.M.; Dauskardt, R.H. Molecular Network Reinforcement of Sol-Gel Glasses. *Adv. Mater.* **2007**, *19*, 3989–3994. [[CrossRef](#)]
25. Kaur, A.; Khanna, A.; González-Barriuso, M.; González, F. Thermal and light emission properties of rare earth (Eu^{3+} , Dy^{3+} and Er^{3+}), alkali (Li^+ , Na^+ and K^+) and Al^{3+} -doped barium tellurite and boro-tellurite glasses. *J. Mater. Sci. Mater. Electron.* **2021**, *32*, 17266–17281. [[CrossRef](#)]
26. Dimitrov, V.; Komatsu, T. Average single bond strength and optical basicity of $\text{Na}_2\text{O-GeO}_2$ glasses. *J. Ceram. Soc. Jpn.* **2009**, *117*, 1105–1111. [[CrossRef](#)]
27. Bih, L.; Omari, M.E.; Réau, J.-M.; Haddad, M.; Boudlich, D.; Yacoubi, A.; Nadiri, A. Electronic and ionic conductivity of glasses inside the $\text{Li}_2\text{O-MoO}_3\text{-P}_2\text{O}_5$ system. *Solid State Ion.* **2000**, *6*, 71–85. [[CrossRef](#)]
28. Ray, N.H. Composition–property relationships in inorganic oxide glasses. *J. Non-Cryst. Solids* **1974**, *15*, 423–434. [[CrossRef](#)]
29. Pershina, S.V.; Antonov, B.D.; Leonidov, I.I. Effect of MoO_3 on structural, thermal and transport properties of lithium phosphate glasses. *J. Non-Cryst. Solids* **2021**, *569*, 120944. [[CrossRef](#)]
30. Fokin, V.M.; Cabral, A.A.; Reis, R.M.C.V.; Nascimento, M.L.F.; Zanutto, E.D. Critical assessment of DTA/DSC methods for the study of nucleation kinetics in glasses. *J. Non-Cryst. Solids* **2010**, *356*, 358–367. [[CrossRef](#)]
31. Rodrigues, A.M.; Narváez-Semanate, J.L.; Cabral, A.A.; Rodrigues, A.C.M. Determination of Crystallization Kinetics Parameters of a $\text{Li}_{1.5}\text{Al}_{0.5}\text{Ge}_{1.5}(\text{PO}_4)_3$ (LAGP) Glass by Differential Scanning Calorimetry. *Mater. Res.* **2013**, *16*, 811–816. [[CrossRef](#)]
32. Rani, S.; Sanghi, S.; Agarwal, A.; Ahlawat, N. Effect of Bi_2O_3 on the dynamics of Li^+ ions in $\text{Li}_2\text{O-P}_2\text{O}_5$ glasses. *J. Mater. Sci.* **2009**, *44*, 5781–5787. [[CrossRef](#)]
33. Jlassi, I.; Sdiri, N.; Elhouichet, H.; Ferid, M. Raman and impedance spectroscopy methods of $\text{P}_2\text{O}_5\text{-Li}_2\text{O-Al}_2\text{O}_3$ glass system doped with MgO . *J. Alloys Compd.* **2015**, *645*, 125–130. [[CrossRef](#)]
34. Mariappan, C.R.; Yada, C.; Rosciano, F.; Roling, B. Correlation between micro-structural properties and ionic conductivity of $\text{Li}_{1.5}\text{Al}_{0.5}\text{Ge}_{1.5}(\text{PO}_4)_3$ ceramics. *J. Power Sourc.* **2011**, *196*, 6456–6464. [[CrossRef](#)]
35. Metwalli, E.E.; Brow, R.K.; Stover, F.S. Cation Effects on Anion Distributions in Aluminophosphate Glasses. *J. Am. Ceram. Soc.* **2001**, *84*, 1025–1032. [[CrossRef](#)]
36. Saout, G.L.; Simon, P.; Fayon, F.; Blin, A.; Vaills, Y. Raman and infrared study of $(\text{PbO})_x(\text{P}_2\text{O}_5)_{1-x}$ glasses. *J. Raman Spectrosc.* **2002**, *33*, 740–746. [[CrossRef](#)]

37. Toloman, D.; Biris, A.R.; Maniu, D.; Bratu, I.; Giurgiu, L.M.; Biris, A.S.; Ardelean, I. Phosphate glassy network depolymerization induced by CaO doping. *Part. Sci. Technol.* **2010**, *28*, 226–235. [[CrossRef](#)]
38. Hudgens, J.J.; Brow, R.K.; Tallant, D.R.; Martin, S.W. Raman spectroscopy study of the structure of lithium and sodium ultraphosphate glasses. *J. Non-Cryst. Solids* **1998**, *223*, 21–31. [[CrossRef](#)]
39. Roiland, C.; Fayon, F.; Simon, P.; Massiot, D. Characterization of the disordered phosphate network in CaO–P₂O₅ glasses by ³¹P solid-state NMR and Raman spectroscopies. *J. Non-Cryst. Solids* **2011**, *357*, 1636–1646. [[CrossRef](#)]
40. Galliano, P.G.; Porto Lopez, J.M.; Varetto, E.L.; Sobrados, I.; Sanz, J. Analysis by nuclear magnetic resonance and Raman spectroscopies of the structure of bioactive alkaline-earth silicophosphate glasses. *Mater. Res. Bul.* **1994**, *29*, 1297–1306. [[CrossRef](#)]
41. Szumera, M. The structural role of manganese ions in soil active silicate–phosphate glasses. *Spectrochim. Acta Part A Mol. Biomol. Spectrosc.* **2014**, *129*, 601–608. [[CrossRef](#)]
42. Sułowska, J.; Wacławska, I.; Olejniczak, Z. Structural studies of copper-containing multicomponent glasses from the SiO₂–P₂O₅–K₂O–CaO–MgO system. *Vib. Spectrosc.* **2013**, *65*, 44–49. [[CrossRef](#)]
43. Tatsumisago, M.; Kowada, Y.; Minami, T. Raman spectra of rapidly quenched glasses and melts containing large amounts of Li₂O. *J. Non-Cryst. Solids* **1992**, *150*, 207–211. [[CrossRef](#)]
44. Belova, E.V.; Kolyagin, Y.A.; Uspenskaya, I.A. Structure and glass transition temperature of sodium-silicate glasses doped with iron. *J. Non-Cryst. Solids* **2015**, *423–424*, 50–57. [[CrossRef](#)]
45. Scott, J.F. Raman Spectra of GeO₂. *Phys. Rev. B* **1970**, *1*, 3488–3493. [[CrossRef](#)]
46. Mernagh, T.P.; Liu, L.-G. Temperature dependence of Raman spectra of the quartz and rutile-types of GeO₂. *Phys. Chem. Miner.* **1997**, *24*, 7–16. [[CrossRef](#)]
47. Sahar, M.R.; Hussein, A.W.M.A.; Hussin, R. Structural characteristic of Na₂O–P₂O₅–GeO₂ glass systems. *J. Non-Cryst. Solids* **2007**, *353*, 1134–1140. [[CrossRef](#)]
48. Osaka, A.; Takahashi, K.; Ikeda, M. Infrared study of trivalent cations B and Fe in amorphous and crystalline phosphates. *J. Mater. Sci. Lett.* **1984**, *3*, 36–38. [[CrossRef](#)]
49. Moreau, F.; Durán, A.; Muñoz, F. Structure and properties of high Li₂O-containing aluminophosphate glasses. *J. Eur. Ceram. Soc.* **2009**, *29*, 1895–1902. [[CrossRef](#)]
50. Pershina, S.V.; Raskovalov, A.A.; Antonov, B.D.; Yaroslavtseva, T.V.; Reznitskikh, O.G.; Baklanova, Y.V.; Pletneva, E.D. Extremal Li-ion conductivity behavior in the Li₂O–Al₂O₃–P₂O₅ glass system. *J. Non-Cryst. Solids* **2015**, *430*, 64–72. [[CrossRef](#)]
51. Kamitsos, E.I.; Yiannopoulos, Y.D.; Karakassides, M.A.; Chryssikos, G.D.; Jain, H. Raman and Infrared Structural Investigation of *x*Rb₂O(1–*x*)GeO₂ Glasses. *J. Phys. Chem.* **1996**, *100*, 11755–11765. [[CrossRef](#)]
52. Kumar, S.; Murugavel, S.; Rao, K.J. Absence of Germanate Anomaly in Ternary Lithium Germanophosphate Glasses: Modification Behavior of Mixed Glass System of Strong and Fragile Formers. *J. Phys. Chem. B* **2001**, *105*, 5862–5873. [[CrossRef](#)]
53. Gandhi, Y.; Rao, M.V.R.; Rao, C.S.; Kityk, I.V.; Veeraiyah, N. Role of Al₂O₃ in upconversion and NIR emission in Tm³⁺ and Er³⁺ codoped calcium fluoro phosphorous silicate glass system. *J. Lumin.* **2011**, *131*, 1443–1452. [[CrossRef](#)]